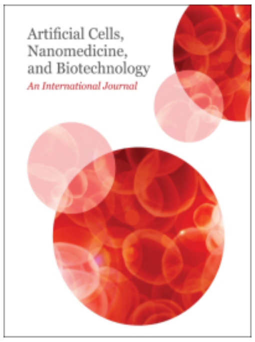

Taylor & Francis
Taylor & Francis Group

Artificial Cells, Nanomedicine, and Biotechnology
An International Journal

ISSN: 2169-1401 (Print) 2169-141X (Online) Journal homepage: www.tandfonline.com/journals/ianb20

Preparation of cell-derived vesicles from eukaryotic and prokaryotic origins for the delivery of biomolecules

Jan Atienza-Garriga, Luke Smithers, Crystal Cooper, Alice Vrielink & Neus Ferrer-Miralles

To cite this article: Jan Atienza-Garriga, Luke Smithers, Crystal Cooper, Alice Vrielink & Neus Ferrer-Miralles (2026) Preparation of cell-derived vesicles from eukaryotic and prokaryotic origins for the delivery of biomolecules, Artificial Cells, Nanomedicine, and Biotechnology, 54:1, 1-18, DOI: 10.1080/21691401.2025.2599072

To link to this article: https://doi.org/10.1080/21691401.2025.2599072

ARTIFICIAL CELLS, NANOMEDICINE, AND BIOTECHNOLOGY
2026, VOL. 54, NO. 1, 1–18
https://doi.org/10.1080/21691401.2025.2599072

Taylor & Francis
Taylor & Francis Group

Preparation of cell-derived vesicles from eukaryotic and prokaryotic origins for the delivery of biomolecules

Jan Atienza-Garriga[a,b,c], Luke Smithers[d], Crystal Cooper[e], Alice Vrielink[d] and Neus Ferrer-Miralles[a,b,c]

[a]Institut de Biotecnologia i de Biomedicina, Universitat Autònoma de Barcelona, Cerdanyola del Vallés, Barcelona, Spain; [b]Centro de Investigación en Red en Bioingeniería, Biomateriales y Nanomedicina, Instituto de Salud Carlos III, Barcelona, Spain; [c]Departament de Genètica i de Microbiologia, Universitat Autònoma de Barcelona, Barcelona, Spain; [d]School of Molecular Sciences, University of Western Australia, Crawley, Western Australia, Australia; [e]Centre for Microscopy, Characterisation and Analysis, University of Western Australia, Crawley, Western Australia, Australia

ABSTRACT
Cell membrane-derived vesicles play essential roles in intercellular communication, material transport, and waste disposal. Despite their biomedical and industrial potential, isolating extracellular vesicles from natural sources remains technically challenging, limiting purification efficiency and scalability. This study introduces cell membrane extrusion as an alternative approach to optimize the production of cell membrane-derived vesicles (CSMs), from eukaryotic and prokaryotic cells. CSMs, generated from HeLa and SH-SY5Y cells exhibited a distinctive cup-shaped morphology and sizes of 151.36 ± 72.36 nm, and 416.86 ± 108.49 nm at 20 °C by DLS respectively, showing remarkable thermal stability at 4-70 °C range. Furthermore, loaded vesicles interacted with mammalian cells and achieved successful cargo internalization. CSMs were also produced from *E. coli* membranes, forming unilamellar vesicles of approximately 100 nm, as observed by Cryo-TEM. These vesicles displayed an inverse correlation between vesicle size and thermal stability and efficient cargo incorporation detected in 85% ± 3% of CSMs. However, under tested conditions, no interaction with prokaryotic cells occurred, and consequently, no delivery of the loaded molecule was observed. Overall, thesefindings highlight the potential of generating cell membrane-derived nanovesicles through extrusion, offering a promising strategy to mimic extracellular vesicles for innovative biomedical and industrial applications, including targeted drug delivery system.

ARTICLE HISTORY
Received 10 June 2025
Revised 21 November 2025
Accepted 29 November 2025

KEYWORDS
Cell-derived vesicles; extracellular vesicles; drug delivery system; protein encapsulation; cell membrane extrusion

Introduction

Cell membrane-derived vesicles from eukaryotic cells, known as extracellular vesicles (EVs), are small, spherical structures encased by lipid bilayers, originating from the cellular membrane [1–4]. These vesicles participate in various physiological and pathological processes, including immune response modulation, cancer progression, and tissue repair [5–7].

In bacterial systems, cell-derived vesicles, referred to as bacterial membrane vesicles (BMVs), are nano-sized, spherical particles released by both Gram-positive and Gram-negative bacteria [8–11]. Research on BMVs offers insights into novel antimicrobial strategies, vaccine development, and biomimetic nanotechnology applications, highlighting their significance in microbiology and biomedicine [10,12].

The inherent biocompatibility, physiochemical stability, and non-immunogenicity of natural extracellular vesicles (EVs) distinguish them as highly promising biological products for advanced drug delivery and theranostic applications, while also serving as efficient carriers for immune checkpoint blockade agents [13,14]. Extracted, for instance, from donated human Mesenchymal Stem Cells (MSCs), EVs offer a cell-free therapeutic platform, presenting a significant advantage over conventional stem-cell-based treatments and opening avenues for personalized medicine [15].

Although natural vesicles hold promising potential for biomedical applications, several critical parameters remain suboptimal. These include the absence of standardized methods for isolation and purification, low efficiency in drug loading, and challenges in achieving

---

CONTACT Neus Ferrer-Miralles neus.ferrer@uab.cat Research Building B (MRB-IBB), UAB Campus, 08193 Barcelona, Spain.

Supplemental data for this article can be accessed online at https://doi.org/10.1080/21691401.2025.2599072.

clinical-grade production [16]. Advanced methods have already helped tackle the challenges of isolating natural EVs and improving throughput by using targeted chemical recognition. Examples include the Amphiphile-Dendrimer Supramolecular Probe system (ADSP array), which enables high-throughput *in situ* protein detection, and Molecularly Imprinted Polymers (MIPs), designed to recognize specific membrane phospholipids and deliver much higher capture efficiency than ultracentrifugation [17–23]. These strategies speed up the process and improve specificity, but they are not without drawbacks. Even platforms built for high throughput struggle with the low concentration of EVs in certain biofluids, such as urine, which often makes sample preconcentration necessary [17,19]. On top of that, affinity-based approaches face scalability issues, with high costs and limited expansion in antibody-based capture remaining a concern. Array-based systems also fall short when it comes to automated sample pre-treatment, which is essential for complex downstream proteomic workflows [17].

An alternative approach involves the generation of cell membrane-derived vesicles, also known as cellsomes (CSMs), through extrusion [24–30], among others. CSMs offer significant advantages as an alternative to exosomes, primarily due to the ability to produce vesicles with a more uniform size distribution, which is crucial for applications requiring precise dosing and predictable biological responses. Additionally, extrusion can be scaled up more easily than natural vesicle purification, making it more feasible for industrial production. This method also reduces the risk of contaminating the vesicle preparations with unwanted cellular components, enhancing the safety profile of vesicle-based products [31]. Related approaches, such as cell-membrane-functionalized nanocarriers, likewise exploit membrane biology for targeting and biodistribution, and are complementary to our extrusion-based strategy [32–35].

Prior work has outlined several strategies to generate mimetic vesicles from cellular membranes [36]. Among these, membrane-extruded cell-derived nanovesicles (CDNVs) reproduce key EV features and have been proposed as practical substitutes for natural EVs [29]. Other approaches include producing nano plasma membrane vesicles (nPMVs) through homogenization of chemically induced blebs, which offer high particle yields and improved uniformity [37], and adapting mechanical extrusion for organ-targeted delivery [30]. Comprehensive reviews summarize these manufacturing strategies and their translational considerations [38]. Building on these foundations, this study introduces a harmonized, cross-kingdom workflow that applies consistent evaluation mètrics, such as size, polydispersity, stability, and functional assays to vesicles derived from both mammalian and bacterial membranes. The protocol integrates practical purification steps, including FACS-based gating and IMAC-based cargo depletion, and sequences established methods to enable side-by-side benchmarking and improve reproducibility across laboratories.

Materials and methods

Cellsomes from animal cells

HeLa cells (ATCC, CCL-2), derived from human cervical adenocarcinoma and classified as epithelial in lineage, were nurtured in Minimum Essential Medium (MEM, Gibco, 12571063) supplemented with 10% Foetal Bovine Serum (FBS, Gibco, 10437028) under a humidified 5% CO_2 atmosphere at 37 °C. SH-SY5Y (ATCC, CRL-2266), originating from human neuroblastoma and exhibiting a neuroblastic lineage, were grown in DMEM/F12 medium (Gibco, 31331093) with10% FBS (Gibco, 10437028) under the same conditions.

Cell Preparation: mammalian cells, reached 100% confluence in 75 ml flasks (~8.4 x 10^6 cells). After trypsinization, 6 ml of MEM was added, and the suspension from two flasks was centrifuged at 500 *g* for 5 min. The supernatant was discarded, and cells were resuspended in 10 ml of PBS, followed by another centrifugation. The pellet was then resuspended in 10 ml of 0.25 X PBS (prepared in Milli-Q water) containing a crushed tablet of cOmplete™, Mini, EDTA-free protease inhibitor cocktail (Roche, Basel, Switzerland) and was incubated on ice for 10 min.

Membrane Disruption: Cells underwent four freeze-thaw cycles, alternating 1 min liquid nitrogen exposure (−196 °C) with 10 min incubation in a 37 °C water bath. Sonication followed for 5 min using a probe sonicator (20 kHz, 30% amplitude), with an ice bath to prevent overheating. Pulses of 30 s ON/OFF minimized thermal damage, totalling 5 min of sonication.

Membrane Purification: The suspension was centrifuged at 700 *g* for 10 min at 4 °C and, discarding the pellet. The supernatant underwent further centrifugation at 15,000 *g* for 30 min at 4 °C yielding a pellet enriched in cytoplasmic membranes. This sequential centrifugation enriches the plasma-membrane fraction and removes most soluble/cytosolic contaminants, constituting an upstream purification step prior to extrusion.

Recombinant eGFP production: Production of recombinant eGFP was performed as previously described [39,40]. Briefly, the codon-optimized GFP-H6 gene was cloned into the pET22b (Amp^R) vector and transformed into *E. coli* BL21(DE3) *via* heat shock (42 °C, 45 s). Cultures (1–2 L) were grown in LB with 100 µg/mL ampicillin at 37 °C, 250 rpm. At $OD_{600} \approx 0.5$, expression was induced with 0.1 mmol/L IPTG and continued overnight at 20 °C. Cells were harvested (5,000 g, 15 min, 4 °C), frozen at −80 °C, then resuspended in wash buffer (20 mM Tris-HCl, 500 mM NaCl, 20 mM imidazole, pH 8.0) with EDTA-free protease inhibitors. Lysis was performed using a high-pressure homogenizer (Avestin Emulsiflex C5, 3 passes). Lysates were clarified (15,000 g, 45 min, 4 °C), and the soluble fraction was purified by Ni^{2+} IMAC on a HisTrap HP column (ÄKTA Pure) using the *N*-lauroylsarcosine–assisted capture workflow, followed by dialysis against 0.01% acetic acid (pH 3.8) and TGX Stain-Free SDS-PAGE quality control and Western blot using anti-6xHis antibody [41]. Protein concentration was determined by UV–Vis at 489 nm using ε_{489} = 55,000 $M^{-1} \cdot cm^{-1}$ with a NanoDrop One spectrophotometer; the stock used here was 1.03 mmol/L. For all loading experiments, eGFP solutions were prepared at 2 µmol/mL from this stock. Gel quality control showed a single predominant band at ~27 kDa with negligible higher-molecular-weight contaminants.

Cellsome Formation: The membrane pellet was resuspended in 1 ml of PBS containing 2 µmol/L recombinant eGFP[39–41].

The sample was vortexed and incubated on ice for 10 min to enhance membrane interaction. It was then extruded 21 times through an extruder (NanoSizer^{TM} extruder, T&T Scientific, Knoxville, TN, USA) using a 400 nm polycarbonate filter. Pilot runs established the final conditions used throughout: extrusion at 4 °C in isotonic buffered saline, with multiple passes at a fixed count to stabilize size distributions; 400 nm polycarbonate membranes were used for mammalian membranes to balance yield and PDI. Preparations were kept on ice and gently mixed to minimize foaming. Upstream pre-clearing spins reduced viscosity and filter clogging. After extrusion, FACS was used to gate size-defined vesicle subpopulations and affinity depletion removed unencapsulated cargo; it does not provide quantitative encapsulation metrics. DLS (hydrodynamic diameter, PDI) served as the selection criterion for acceptable runs (low PDI, reproducible Z-average), and these settings were then kept constant across all replicates.

We selected extrusion for vesicle formation due to its equipment-light, reproducible workflow and the ability to preserve membrane proteins relevant to uptake; more aggressive approaches (e.g. cavitation or extended sonication) were confined to upstream membrane liberation rather than vesicle shaping in order to minimize protein denaturation [29,34,42].

For all downstream assays, CSM preparations were used fresh whenever possible; when storage was necessary, samples were kept at 4 °C, protected from light, and were not subjected to freeze–thaw cycling.

Cellsomes from bacterial cells

For cellsome production from bacterial cells, BL21 (DE3) pLEMO *E. coli* cells (Lemo21(DE3)) were used [39], grown in 1 mM rhamnose to facilitate cell wall degradation.

Bacterial Cell Preparation: A single colony of *E. coli* Lemo21(DE3) (New England Biolabs, Ipswich, MA, USA) was resuspended in a 50 ml LB containing 30 µg/ml chloramphenicol. This was done in duplicate.

Growth and harvesting: Cells were grown overnight at 37 °C with 200 rpm shaking and 1 mM of L-rhamnose. Following induction, the 100 ml culture (OD_{600} 5.5; 8.8 x 10^9 cells) was centrifuged at 4000 g for 5 min, discarding the supernatant. PBS was added, followed by a second centrifugation step.

Lysozyme Treatment and Freezing: Cells were incubated in PBS with 10 mg/mL lysozyme for 30 min at 37 °C with agitation, then centrifuged at 500 g for 5 min. The supernatant was removed and the pellet homogenized in PBS before immediate freezing in liquid nitrogen.

Membrane processing and CSM Formation: Membrane disruption, purifications, and CSM formation followed the protocol described in the previous section using 100 nm polycarbonate extruder (T&T Scientific). After extrusion, the membrane pellet was resuspended in extrusion buffer with recombinant eGFPH6 and mRUBYH6.

Confocal microscopy experiments of mammalian cells incubated with CSMs

HeLa cells and SHSY-5Y cells were seeded onto 35 mm Ibidi glass-bottom plates (Ibidi GmbH, Gräfelfing, Germany) at 40-50% confluency. Nuclei were labelled with 0.2 µg/mL Hoechst 33342 (Molecular Probes, Eugene, OR, USA) for 10 min in the dark. Subsequently, 50 µL of HeLa cellsomes were added directly without dilution, requiring no further incubation.

Images were captured using a ZEISS LSM 980 confocal laser scanning microscope equipped with Airyscan 2 (Carl Zeiss GmbH, Oberkochen, Germany). Given the small sample size, images were acquired utilizing the Airyscan detector, enabling the collection of fluorescence signals in distinct and independent channels. Specifically, a plasma membrane stain (CellMask Deep Red) was excited at 639 nm, with emission collected at 300–720 nm, while eGFP fluorescence was excited at 488 nm, with emission at 495–550 nm. To faithfully represent the sample composition prior to purification, images in Figure 1 were acquired with identical laser power, detector gain, and display ranges across groups, and no background subtraction or non-linear contrast operations were applied. For Figure 5, images were acquired at $t=0$ and 60 min (soluble GFP) and $t=0$ and 30 min (GFP-CSMs). No full time-lapse was collected and no kinetic analysis was performed. A subset of samples was inspected by Z-stack acquisition for visual assessment only; no extracellular quenching/stripping or protease-protection assays were performed in this study.

Cellsome purification by cell sorting and affinity chromatography

Immediately after extrusion, vesicle suspensions were purified to (i) remove debris and large aggregates, (ii) isolate size-defined vesicle subpopulations, and (iii) deplete unencapsulated cargo, as detailed in Materials and Methods Sections Flow cytometry and cell sorting and Affinity chromatography.

Flow cytometry and cell sorting

Flow cytometric analysis on CSM samples was conducted using a CytoFLEX LX flow cytometer (Beckman Coulter, Brea, CA, USA), detecting GFP fluorescence in the FITC channel (525/40 filter) with 488 nm laser. Data was processed using CytExpert software (Beckman Coulter). A BD FACSJazz cell sorter (BD Biosciences, Franklin Lakes, NJ, USA) with 488 nm and 635 nm lasers sorted cells, configured to detect GFP fluorescence in the FITC channel (530/40 filter) at a flow rate to optimize detection of small particles. Sorted fractions were collected into pre-cooled tubes and immediately re-analysed by flow cytometry to verify gate fidelity before downstream use.

Populations were gated using forward and side scatter (FSC/SSC) scatter to remove debris. Sorting was based on size into three categories: small, big, and superbig. Green fluorescence was not used for gating due to interference from other green particles (e.g. membranes, aggregated GFP). At least 150 particles per group were sorted using the purity mode.

Data analysis was conducted with BD Sortware software (BD Biosciences), incorporating negative controls

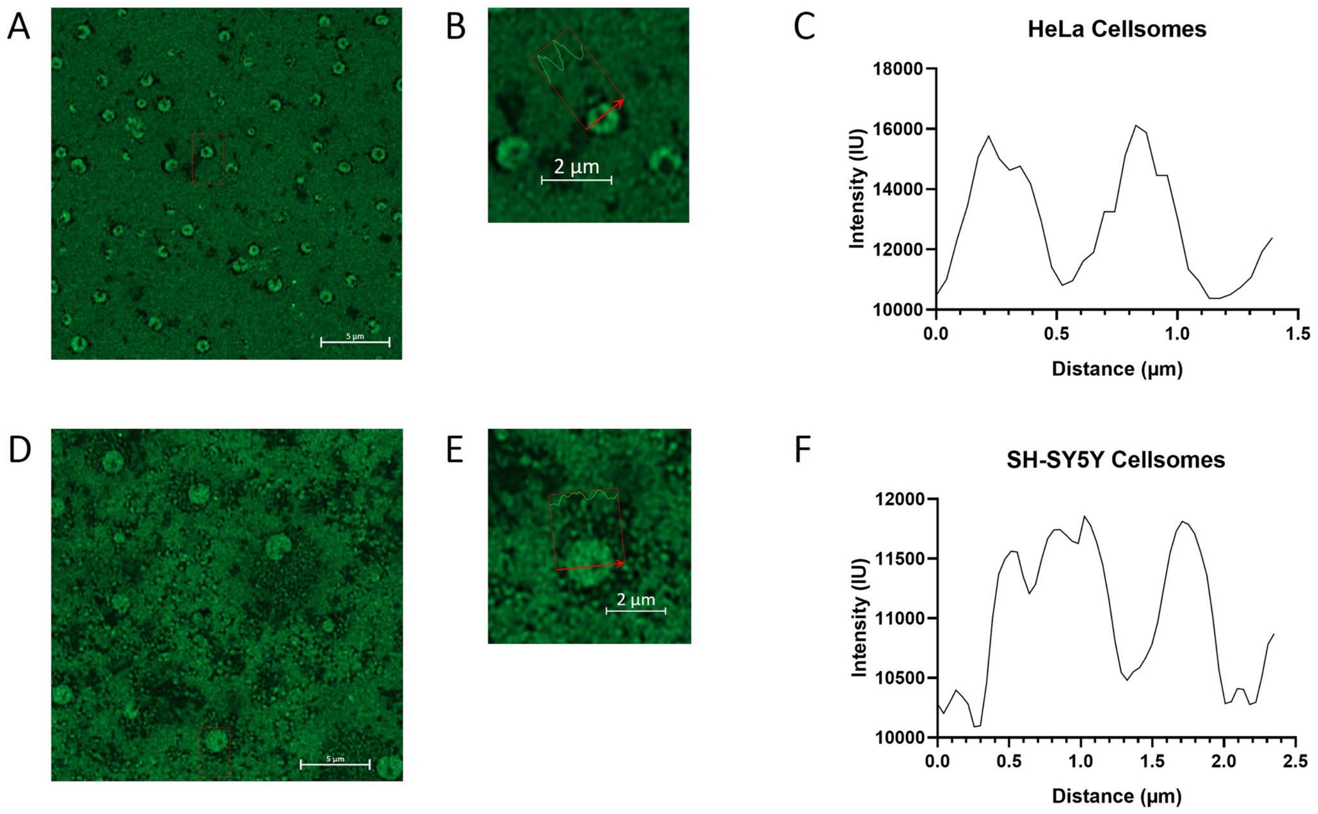

Figure 1. LSCM images of cell membrane-derived vesicles (CSMs) extruded with 2 µmol/L GFP. (a) General image of CSMs from HeLa cells. (b) Image amplification of one CSM from HeLa cells. (c) Fluorescence profile of the isolated CSM from HeLa cells of panel (b). (d) General image of CSMs from SH-SY5Y cells. (e) Image amplification of one CSM from SH-SY5Y cells. (f) Fluorescence profile of one isolated CSMs from SH-SY5Y cells. Green fluorescence signal of GFP associated with CSMs was recorded (λ_{ex} = 488 nm, λ_{em} = 495–550 nm). Scale bar (a) and (d): 5 µm; (b) and (e) 2 µm.

(GFP and dilution buffer) to validate gating strategies and instrument sensitivity.

Affinity chromatography

To remove unencapsulated eGFPH6 and mRUBYH6 from cellsomes, affinity chromatography step was performed using empty columns (Econo-Pac® columns, Bio-Rad Laboratories, Inc, Hercules, CA, USA) packed with 2 ml of affinity resin (Talon® Superflow™ resin, ref. 28-9575-02, Cytiva, Marlborough, MA, USA). To deplete unencapsulated His-tagged recombinant proteins, vesicle suspensions were passed over Co^{2+}-charged IMAC resin; free His-tagged proteins were retained on the matrix, whereas the vesicle-containing flow-through was collected and used for subsequent assays. The purification with sequential washes: 10 ml distilled water, followed by 10 ml PBS. Subsequently, 1 ml of impure cellsomes was loaded onto the column, washed with 1 ml PBS, and the flow-through collected as purified cellsomes. The bound sample was eluted using buffer (20 mM Tris HCl, pH 8/500 mM NaCl/500 mM Imidazole). This depletion step removes non-encapsulated cargo but does not distinguish lumenal cargo from peripherally adsorbed cargo on the vesicle surface.

Cellsomes visualization in Cryo-TEM

For Cryo-TEM visualization, samples were prepared using a Leica GP 2 automatic plunge freezer (Leica Biosystems, Wetzlar, Germany) at 4 °C and 95% humidity. Following extrusion, CSMs were purified with Ni Sepharose High Performance histidine-tagged protein purification resin (ref. 17526801, Cytiva, Marlborough, MA, USA). 3 µl of purified bacterial cellsomes were applied to a glow-discharged holey carbon grid (Quantifoil copper R 2/2, 200 mesh). Subsequently, the sample was blotted for 4 s to remove excess liquid before plunge freezing in liquid ethane. The grid was then transferred to a JEOL JEM-F200 cryo-electron microscope (JEOL Ltd., Akishima, Japan) and imaged at 200 kV using a Gatan RIO detector. Prior to vitrification, preparations were briefly incubated with Ni-Sepharose High Performance resin to capture residual His-tagged proteins; the vesicle-enriched supernatant was recovered for imaging. This additional cleanup reduces proteinaceous background and constitutes a downstream purification step. Cryo-TEM was chosen over negative staining to avoid dehydration-related artefacts (e.g. vesicle collapse/flattening) and to preserve native hydrated morphology; consequently, image contrast is lower than in stained EM. Contrast and brightness settings were uniformly applied across all panels.

DLS size determination and thermal stability of cellsomes

The homogeneity of CSM populations obtained *via* extrusion, described in the sections Cellsomes from Animal Cells" and Cellsomes from Bacterial Cells, was assessed using Dynamic light scattering (DLS) analysis with a Zetasizer Nano ZS instrument (Malvern Panalytical, UK), at 633 nm. This method provided a volume-weighted size distribution and polydispersity index (PDI), indicating sample uniformity. A PDI below 0.2 signified a monodisperse sample. Analyses were conducted in triplicate, with vesicle suspensions equilibrated at 25 °C for 3 min before measurements. We report the Z-average hydrodynamic diameter (D_h) and PDI (mean ± SD); size-distribution plots in Figure 3(a, c, and e) show the corresponding volume distributions provided by the instrument; these quantitative sizes are the reference for vesicle dimensions in this study.

CSM thermal stability was evaluated across a temperature range of 4- 70 °C, with measurements performed at intervals of 4, 10, 20, 25, 30, 37, 40, 50, 60, and 70 °C. Each measurement was preceded by a 180-s incubation to ensure equilibration. Stability was determined based on size consistency and the absence of significant PDI increases, which would indicate vesicle aggregation or structural disruption.

Zeta potential was measured by electrophoretic light scattering using Zetasizer Nano ZS instrument (Malvern Panalytical, UK) at 25 °C. All samples were measured at least in triplicate, and data are expressed as mean ± standard error.

All determinations were performed using vesicle samples that had been prepared less than seven days prior to analysis, considering that natural extracellular vesicles generally maintain relative stability when stored at 4 °C for short durations, typically spanning several days to a few weeks [43].

Confocal microscopy experiments on bacterial cells incubated with CSMs

To visualize *E. coli* pLEMO cells incubated with CSMs, samples were stained and prepared under specific conditions. Bacterial DNA was labelled with 0.2 µg/mL Hoechst 33342 (Molecular Probes, Eugene, OR, USA) and a plasma membrane dye at 2.5 µg/mL (CellMask™ Orange, Molecular Probes), both incubated for 10 min in the dark. Then, 100 µL of undiluted *E. coli* pLEMO CSMs were applied directly to microscope slides (Corning® microscope slides, Sigma-Aldrich, CLS294875X25). A 1:10 dilution from an OD_{600} of 0.2 was used for bacterial visualization.

Imaging was performed using a Leica SP5 (Leica Biosystems, Wetzlar, Germany) confocal scanning microscope equipped with a 405 nm diode laser, an Argon laser at 488 nm, and a 561 nm diode-pumped solid-state (DPSS) laser. Hoechst-stained DNA was excited at 405 nm (emission: 430–490 nm) and CellMask Orange was excited at 561 nm (emission: 300–720 nm). GFP-tagged CSMs were excited at 488 nm with emission detected at 500–560 nm. All channels were acquired under conservative, identical laser/detector settings to avoid saturation and bleed-through, and no nonlinear background subtraction was applied. Quantification of GFP enrichment within CellMask-positive vesicle ROIs is reported in Figure S1A as bar-with-scatter.

Confocal images were analysed using ImageJ software (NIH) to determine the colocalization between GFP (488 nm excitation, 510 nm emission) and CellMask Orange (561 nm excitation, 590 nm emission). The Pearson correlation coefficient (PCC) was calculated *via* Coloc2 with automatic threshold settings. Colocalization was measured as the ratio of overlapping fluorescence pixels to total red fluorescence pixels per field of view. Three independent samples were analysed, with at least five images per sample. Images were acquired with identical settings. Vesicle ROIs were obtained from the CellMask channel (Otsu thresholding, hole filling, watershed; size filter 0.05–2.0 μm^2, circularity 0.2–1.0). For each ROI, mean GFP was measured and a local background was computed from a 2–4 px annulus excluding neighbouring ROIs. A vesicle was classified as GFP-overlapping if mean (GFP_ROI) > bg_mean + 3 × bg_SD. For each field, the fraction overlapping = (# overlapping/# total vesicles). We report n fields = 2, nROIs = 110; per-field values are 92.6% and 83.1% (mean ± SD 87.9% ± 6.7%); overall fraction (weighted by ROIs) 85.5%. ROI-level CSVs and overlays are provided in the repository.

Transformation of bacterial cells with CSMs

Plasmid DNA incorporation was performed by mixing the membrane preparation with a plasmid DNA solution (1.65 ng/mL in PBS, pH 7.4). Extrusion was carried out using 400 nm filters with purified plasmids pET22GFP 41 and pETmRUBY (Addgene plasmid # 86934).

Plasmids were purified using the NZYMiniprep kit (Nzytech, Lisbon, Portugal). Briefly, *E. coli* BL21(DE3) cells transformed with pET22GFP or pETmRUBY were cultured in LB with 100 µg/mL ampicillin at 37 °C, 200 rpm overnight. Plasmid DNA was extracted following the manufacturer's protocol, including alkaline lysis and silica column purification. DNA was eluted in 50 µL Tris-HCl (10 mM, pH 8.5) and quantified *via* NanoDrop (Thermo Fisher), yielding 500–800 ng/µL.

The membrane-DNA mixture was homogenized by pipetting for 1 min and incubated at room temperature for 15 min to facilitate interaction. Following DNA loading, samples were treated with DNase I to digest non-encapsulated plasmid and then washed by centrifugation (15,000 *g*, 30 min, 4 °C) to remove the enzyme and degradation products, thereby minimizing free DNA in the final preparations.

The suspension was extruded through a 400 nm polycarbonate Nanosizer filter (T&T Scientific, Knoxville, TN, USA) using 21 cycles under moderate pressure to ensure vesicle formation and encapsulation while preserving membrane integrity. DNase I (1 U/µL, Thermo Fisher Scientific) was then added to degrade any unencapsulated plasmid DNA, followed by incubation at 37 °C for 1 h with gentle agitation (100 rpm). Negative controls consisted of bacterial CSMs without plasmid DNA.

Extruded CSMs were washed by centrifugation (15,000 g, 30 min, 4 °C) to remove excess DNase and degradation products, then resuspended in fresh PBS and stored at 4 °C. Encapsulation efficiency was assessed through confocal microscopy (see Section Confocal microscopy experiments on bacterial cells incubated with CSMs) and dynamic light scattering (DLS, see Section DLS size determination and thermal stability of cellsomes).

DNA-loaded CSMs (100 µL) were incubated with 900 µL of *E. coli* competent cells (OD_{600} 0.6) at 37 °C for 2 h with gentle agitation (150 rpm) before heat shock treatment. Transformed cells were seeded on LB-agar plates with ampicillin (100 mg/mL, pET22GFP) or kanamycin (50 mg/mL, pETmRuby).

In parallel to CSM-mediated transformations, the assay was validated with standard controls. Positive control: chemically competent *E. coli* BL21(DE3) cells subjected to $CaCl_2$ heat-shock transformation with the same mass of pGFP plasmid DNA used in the CSM condition (42 °C, 45 s; recovery 1 h in SOC; plate on LB + Amp). Negative controls: (i) CSMs prepared without DNA; (ii) DNase-treated CSMs (incubation with DNase I in the presence of Mg^{2+}, followed by EDTA quench/heat inactivation) processed identically. These controls are standardized procedures and are referenced to established protocols [44]. Control plates are not shown, as Figure 8 focuses on the CSM condition.

Statistical analysis

All experiments included at least three independent replicates, with data presented as mean ± standard deviation (SD). For comparisons of vesicle size and stability across different conditions, one-way analysis of variance (ANOVA) was performed, followed by Tukey's post-hoc test for pairwise comparisons. Statistical significance was set at $p < 0.05$. The software used for statistical analysis was GraphPad Prism 9 (GraphPad Software, San Diego, CA, USA).

Image analysis

Image analysis was performed in Fiji and Python/NumPy with identical parameters across groups. For Figure 7, CellMask images were lightly smoothed and thresholded to segment vesicle ROIs; for each ROI we measured GFP mean intensity and a local background annulus (2–4 px) to compute S/B ratio = mean (ROI)/mean(background). For Figure 8, vesicle puncta were segmented from the relevant channel (GFP or CellMask) and S/B ratio was computed analogously; a puncta-per-field count is also reported. Data are shown as bar-with-scatter (all points visible); acquisition and display settings were identical, and no nonlinear background subtraction was applied.

Results

Characterization of extruded cell membranes from eukaryotic cells

CSMs were generated from HeLa and SH-SY5Y cell membranes *via* extrusion through a 400 nm pore size filter with recombinant GFP. Laser Scanning Confocal Microscopy (LSCM) revealed a unique cup-shaped morphology, with HeLa-derived CSMs measuring 1,130 ± 110 nm ($n = 10$) and SH-SY5Y-derived CSMs at 1,740 ± 190 nm ($n = 7$) (Figure 1a, d). Fluorescence intensity profiles showed a central reduction, more pronounced in SH-SY5Y-derived CSMs, which had a smaller central gap compared to HeLa CSMs (Figure 1c, f). At this pre-purification step, soluble GFP remains in the medium and appears as diffuse background, while vesicle-associated GFP is visible as rim-labelled rings and bright puncta (Figure 1). Background was not subtracted to avoid removing true soluble signal present at this stage; all panels share identical acquisition and display settings. The subsequent purification workflow removes the soluble fraction, as decribed in the Materials and Methods section on Cellsome purification by cell sorting and affinitychromatography. These LSCM images are used qualitatively to visualize GFP-associated vesicles on glass; the apparent widths obtained from line profiles reflect diffraction-limited optical features of rim-labelled vesicles and are not used for size determination.

HeLa CSM purity was assessed through fluorescence-activated cell sorting, identifying three populations: small, big, and superbig (Figure 2a, b). Confocal microscopy showed large aggregates in the superbig population, while no fluorescent CSMs were detected in the small or big groups (Figure 2c). SH-SY5Y CSMs lacked distinct populations based on fluorescence intensity, and LSCM imaging did not reveal observable CSMs.

Quantitative sizing was therefore obtained by dynamic light scattering (DLS), which reports the hydrodynamic diameter (D_h) of vesicles in suspension together with the polydispersity index (PDI) (Figure 3). These DLS/PDI readouts were used to select the final pore sizes and pass number, which were then fixed for all experiments reported here. Dynamic Light Scattering (DLS) analysis indicated HeLa-derived CSMs (superbig population) averaged 151.36 ± 72.36 nm at 20 °C, while SH-SY5Y CSMs measured 416.86 ± 108.49 nm (Figure 3a, c). Differences between the apparent optical diameters in LSCM and the hydrodynamic diameters from DLS are expected because the two modalities probe different physical quantities and sample states. As previously described for extracellular vesicles, Zeta potentials of CSMs at pH 7.4 were mildly negative in all cases: HeLa −5.8 ± 1.5 mV, SH-SY5Y −4.6 ± 0.2 mV, and E. coli −4.0 ± 0.9 mV [15]. We evaluated thermal stability by DLS over a temperature range of 4–70 °C (Figure 3b, d, f) to characterize vesicle robustness under thermal stress. Quantitative size measurements are reported as hydrodynamic diameters (D_h), accompanied by corresponding PDI values. Thermal stability assessments showed HeLa CSMs remained stable across the tested temperature range, with minimal size reduction above 60 °C (Figure 3b). SH-SY5Y CSMs exhibited increasing size with temperature, with slight shrinkage around 30 °C (Figure 3d).

Characterization of extruded cell membranes from prokaryotic cells

Bacterial CSMs were generated from *E. coli* BL21(DE3) membranes using a 100 nm pore size filter and observed by Cryo-Transmission Electron Microscopy (Cryo-TEM). Cryo-TEM grids were prepared from the post-extrusion Ni^{2+}-affinity–purified fraction, detailed in the Materials and Methods section on Cellsomes characterization in Cryo-TEM, which captures residual His-tagged proteins and reduces proteinaceous background. Cryo-TEM imaging revealed unilamellar vesicles with an average size of ~100 nm, consistent with bacterial CSM morphology (Figure 4).

In contrast, DLS measurements in Figure 3 were acquired on the bulk suspension before this purification step; thus, Cryo-TEM and DLS probe differently cleaned preparations, explaining cleaner fields in Figure 4 and differences in apparent sizes. In fact,

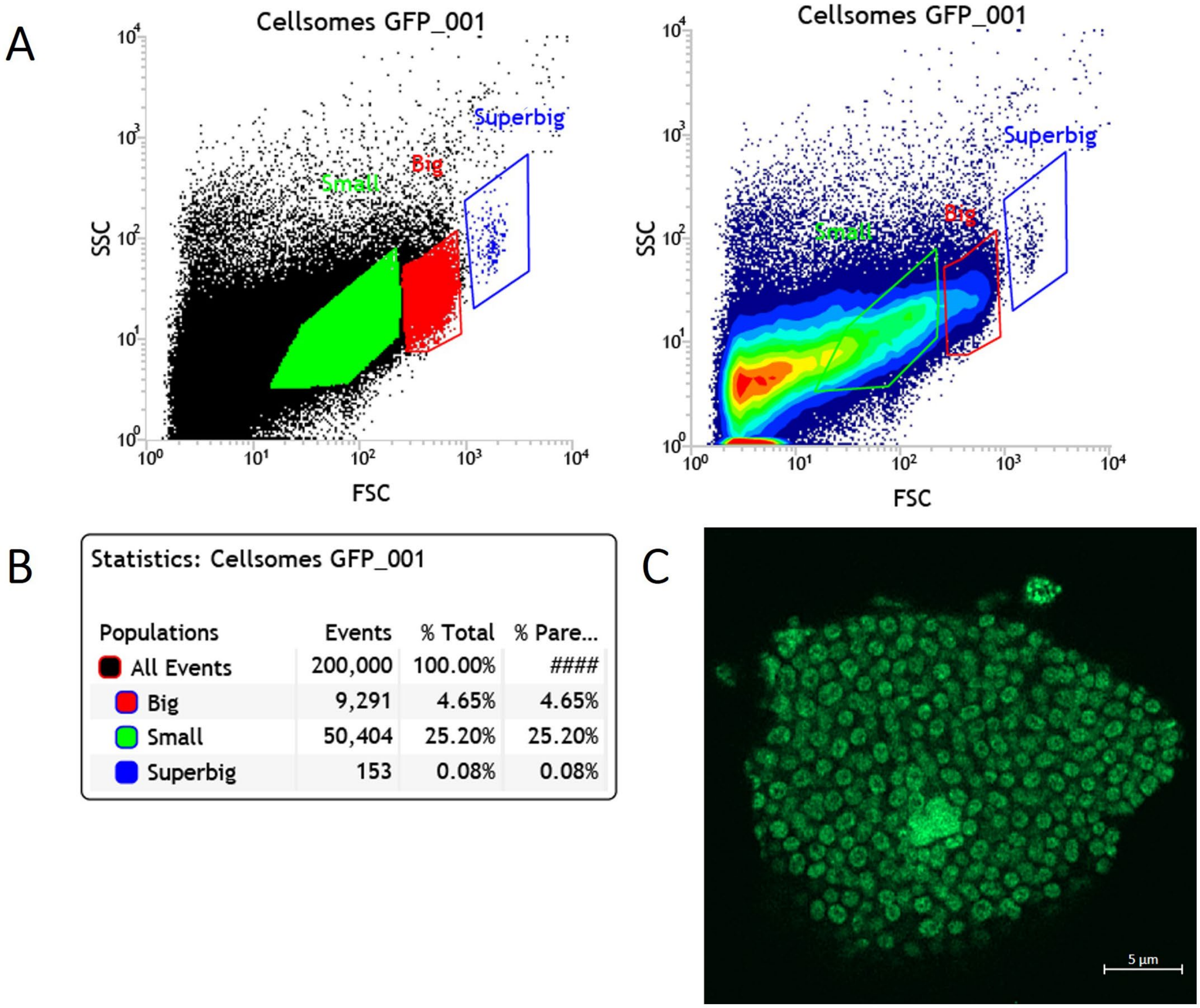

Statistics: Cellsomes GFP_001

Populations	Events	% Total	% Pare...
⬛ All Events	200,000	100.00%	####
🟥 Big	9,291	4.65%	4.65%
🟩 Small	50,404	25.20%	25.20%
🟦 Superbig	153	0.08%	0.08%

Figure 2. Flow cytometry coupled to cell sorting applied to CSMs from HeLa cells extruded with 2 µmol/L GFP. (a) Three different subpopulations were isolated and marked by coloured boxes (small, big, and superbig events). (b) Percentage of the isolated CSM subpopulations of cell membrane-derived vesicles. (c) LSCM image of one superbig event. Extrusion was performed using 400 nm polycarbonate filters. GFP fluorescence was recorded (λ_{ex} = 488 nm, λ_{em} = 500–560 nm). Sorting gates were set based on forward and side scatter (FSC and SSC) to separate subpopulations. Sacale bar 5 µm.

DLS analysis at 20 °C showed an average size of 879.12 ± 232.14 nm. Thermal stability assessments tracked size variations across various temperatures, revealing an inverse size-temperature correlation, except for slight increases around 30 °C (Figure 3e, f).

Interaction of CSMs from eukaryotic cells with HeLa cells

The interaction between HeLa-derived CSMs loaded with GFP and HeLa cells was assessed by LSCM. As a control, exponentially growing HeLa cells were incubated with soluble GFP. At 0 min, fluorescence was detected only in the medium, indicating no cell interaction. After 60 min, green fluorescence dots appeared inside the cells, suggesting GFP uptake into the cytoplasm (Figure 5a, b). When HeLa cells were exposed to GFP-loaded CSMs, fluorescence was immediately visible on the cell surface and within the cells, indicating rapid interaction and possible uptake (Figure 5c). At extended time points, fluorescence was consistently detected inside the cells (Figure 5d). We observe cell-associated GFP signal compatible with internalization; however, as no extracellular quenching or surface-stripping controls were performed, we cannot exclude a contribution from vesicles adhered to the plasma membrane. These images are shown as qualitative endpoints; intermediate time points were not acquired, so we do not report kinetics.

Closer inspection of the cell membranes revealed bright fluorescence spots at specific surface locations (Figure 6a). Magnified images showed structures consistent with CSM-cell interaction points (Figure 6b, d, f). Fluorescence profiles from these regions matched

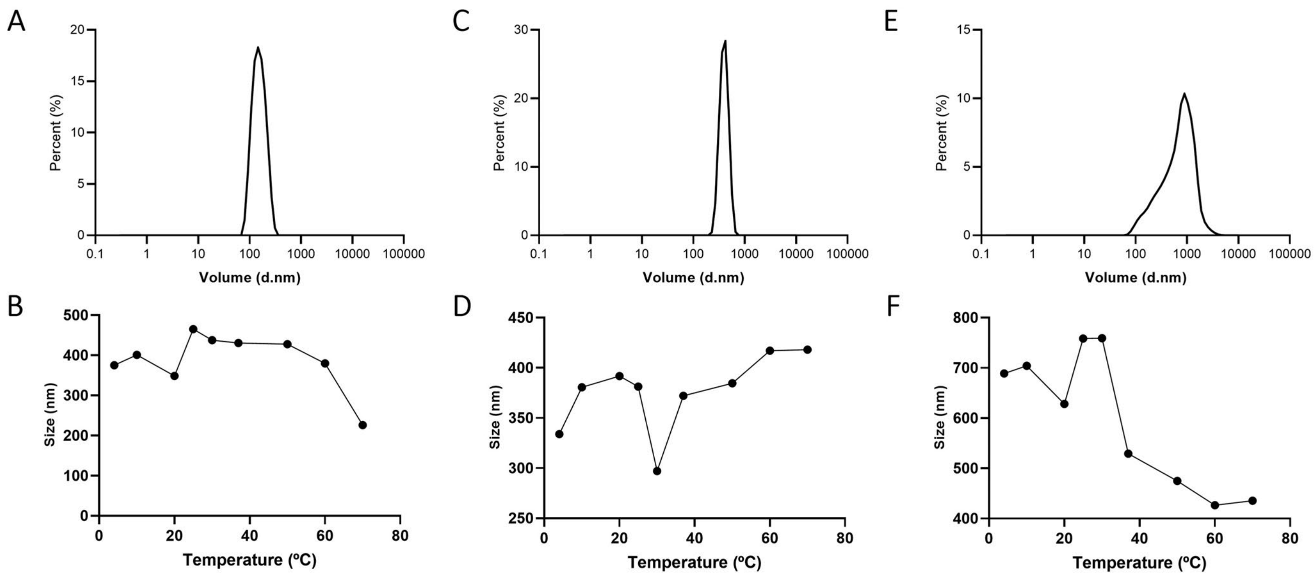

Figure 3. DLS analysis of CSMs from cell membranes. (a) Size Distribution of CSMs obtained from HeLa cells at 25 °C. (b) Thermal stability of CSMs from HeLa cells. (c) Size Distribution of CSMs obtained from SH-SY5Y cells at 25 °C. (d) Thermal stability of CSMs from SH-SY5Y cells. (e) Size distribution of CSMs obtained from *E. coli* cells at 25 °C. (f) Thermal stability of CSMs from *E. coli* cells.

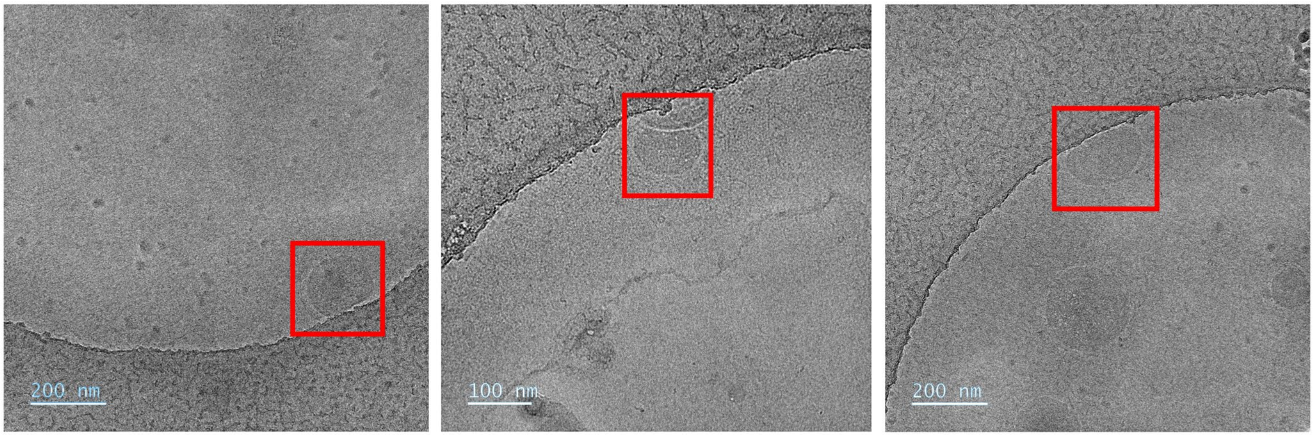

Figure 4. Cryo-TEM Bacterial CSMs. Representative images of purified CSMs obtained from E. *coli* cell membranes. CSMs are highlighted within red squares to indicate their structure and morphology. Extrusion was performed using 100 nm polycarbonate filters. Images were acquired by cryo-TEM from the post-extrusion Ni^{2+}-affinity–purified flow-through (see Materials and Methods section Cellsomes visualization in Cryo-TEM). Representative fields are shown; scale bars as indicated. Vitrified samples without staining. Contrast and brightness settings were uniformly applied across all panels. Insets highlight representative membrane bilayers to facilitate visualization. Scale bars 100 nm and 200 nm.

patterns observed in isolated CSMs (Figure 1c, f), confirming attachment and potential internalization. Due to purification challenges, full characterization *via* confocal microscopy was not conducted for SH-SY5Y-derived CSMs.

Interactions of CSMs from prokaryotic cells with E. coli

CSMs derived from *E. coli* membranes and loaded with GFP were stained with a plasma membrane dye (CellMask Orange) for visualization. LSCM imaging revealed discrete red spherical structures corresponding to the stain, along with green fluorescence from GFP (Figure 7).

Colocalization appeared as yellow signals, confirming GFP presence within CSMs (Figure 7a–cC). Analysis showed 85% ± 3% of CSMs exhibited overlapping GFP and CellMask Orange fluorescence, with a Pearson correlation coefficient (PCC) of 0.85 ± 0.03, indicating efficient GFP incorporation and minimal leakage or aggregation. Fluorescence profiles supported vesicle integrity. To summarize these observations, GFP S/B ratio within CellMask-positive vesicle ROIs from the same fields is reported in Figure S1A. The GFP channel

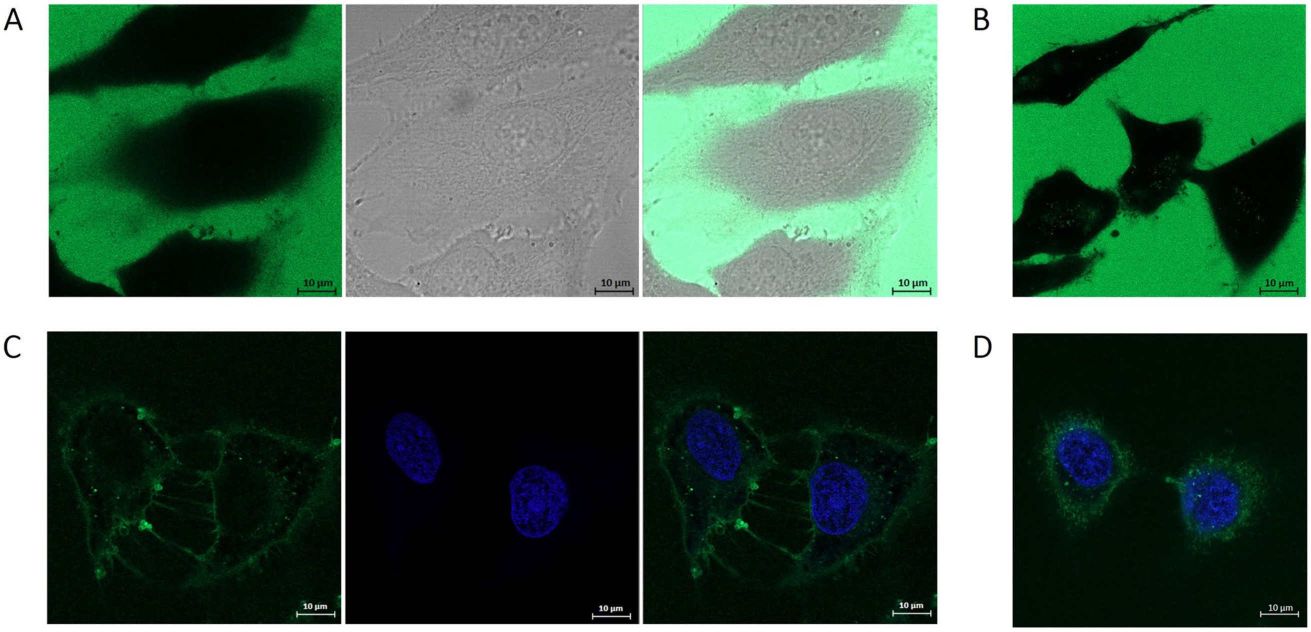

Figure 5. LSCM images of HeLa cells incubated with GFP or loaded GFP-CSMs. (a) HeLa cells incubated with soluble 2 µmol/L GFP at 0 min. (b) confocal fluorescence microscopy image of the same cells at 60 min. (c) HeLa cells incubated with GFP-CSMs at 0 min. (d) HeLa cells incubated with GFP-CSMs at 30 min. The series includes confocal fluorescence microscopy images, bright field images, and merge images. Green fluorescence: GFP; blue fluorescence: Hoechst. GFP fluorescence was recorded at λ_{ex} = 488 nm and λ_{em} = 495–550 nm. Hoechst fluorescence was recorded at λ_{ex} = 405 nm and λ_{em} = 430–470 nm. Scale bar 10 µm.

appears dimmer than CellMask because cargo is present at low copy number within diffraction-limited vesicles. Images were acquired with identical settings and without nonlinear background subtraction to preserve comparability. The ROI-based quantification from these same fields shown in Figure S1A (GFP signal-to-background ratio within CellMask-positive ROIs) demonstrates that the GFP signal is specific.

To assess CSMs interaction with bacterial cells, GFP-labelled CSMs were incubated with *E. coli*, whose DNA was stained with Hoechst. The bacterial suspension displayed evenly distributed cells with blue fluorescence. Upon CSMs addition, green fluorescence surrounded bacteria, suggesting proximity. However, no colocalization between GFP and bacterial DNA was observed, indicating CSMs did not achieve direct internalization (Figure 8). A descriptive comparison of S/B ratio for the two conditions and a puncta-density proxy are shown in Figure S1B-C.

Transformation experiments tested whether CSMs could deliver plasmid DNA into *E. coli*. Membranes were extruded with pET expression vectors encoding GFP and Ruby proteins. After incubating with competent *E. coli* cells, transformation mixtures were plated on LB agar with selective antibiotics. No colonies formed under any tested condition, suggesting CSMs did not facilitate plasmid DNA uptake in these experimental settings. Given the DNase pre-treatment used to remove non-encapsulated plasmid prior to exposure (see Materials and Methods section Transformation of bacterial cells with CSMs), these negative outcomes argue against spurious uptake from free DNA and instead point to limitations in vesicle–cell interaction and/or intracellular release.

Discussion

Extracellular vesicles (EVs) play a crucial role in cell-to-cell communication and regulation of physiological processes in both eukaryotic and prokaryotic organisms. Natural bacterial vesicles encapsulate proteins, genomic DNA, and plasmid DNA, protecting them from degradation and facilitating transfer to recipient bacterial cells [45–47]. Their biomedical potential has gained attention, with applications in biomarker discovery, targeted drug delivery, tissue regeneration, nanovaccines, diagnostics, and cancer immunotherapy [6,7,16].

EVs enter cells through multiple endocytic pathways, influenced by surface proteins and glycoproteins. Multiple routes can be used simultaneously, explaining why blocking a single pathway doesn't fully prevent entry. Membrane-derived vesicles obtained through extrusion may mimic EV interactions with cells, offering enhanced encapsulation efficiency and a controlled production process.

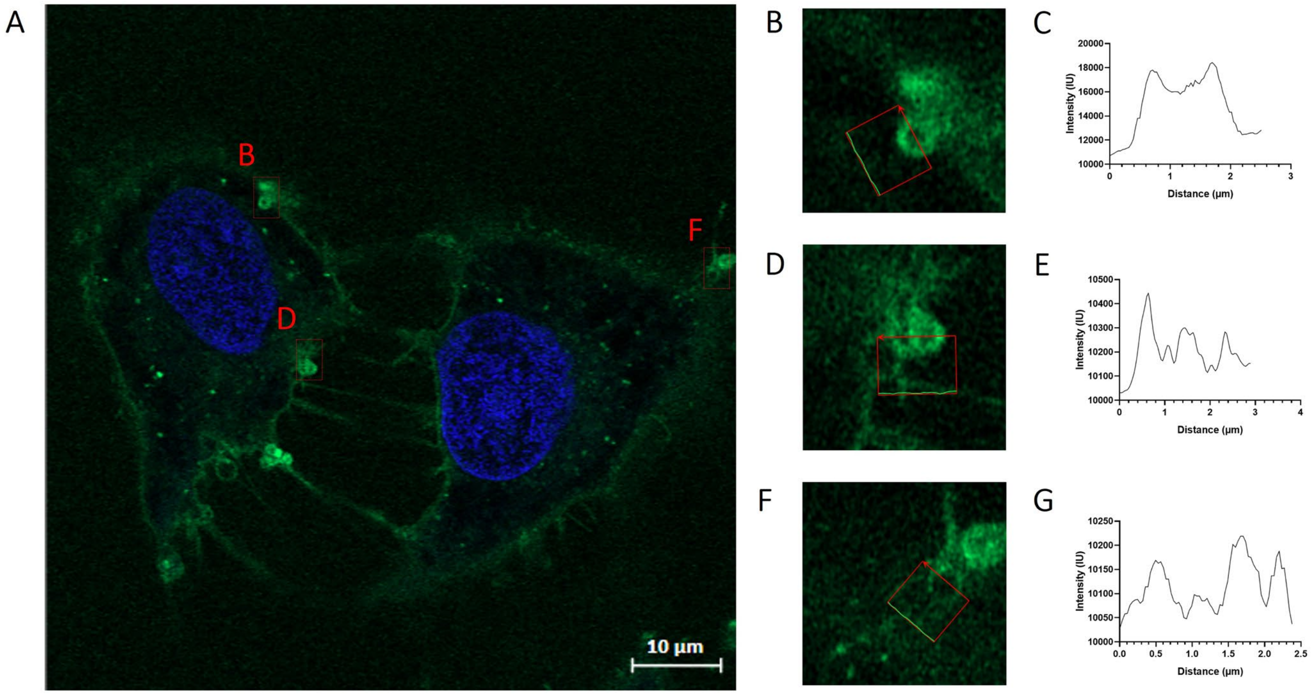

Figure 6. LSCM (Laser Scanning Confocal Microscopy) images of HeLa cells showing CSM interaction points. (a) Broad view of two HeLa cells with marked areas (numbered 1, 2, and 3) indicating regions of interest for closer examination of CSM interaction points. (b, d, f) Close-up images of the respective areas marked in A (1 = B, 2 = D, 3 = F). (c, e g) Fluorescence intensity profiles corresponding to the red square regions in B, D, and F. Each graph plots the intensity of fluorescence across the area, providing quantitative data supporting the visual observations of CSM attachment. GFP fluorescence was recorded at λ_{ex} = 488 nm and λ_{em} = 495–550 nm. Hoechst fluorescence was recorded at λ_{ex} = 405 nm and λ_{em} = 430–470 nm. Scale bar 10 µm.

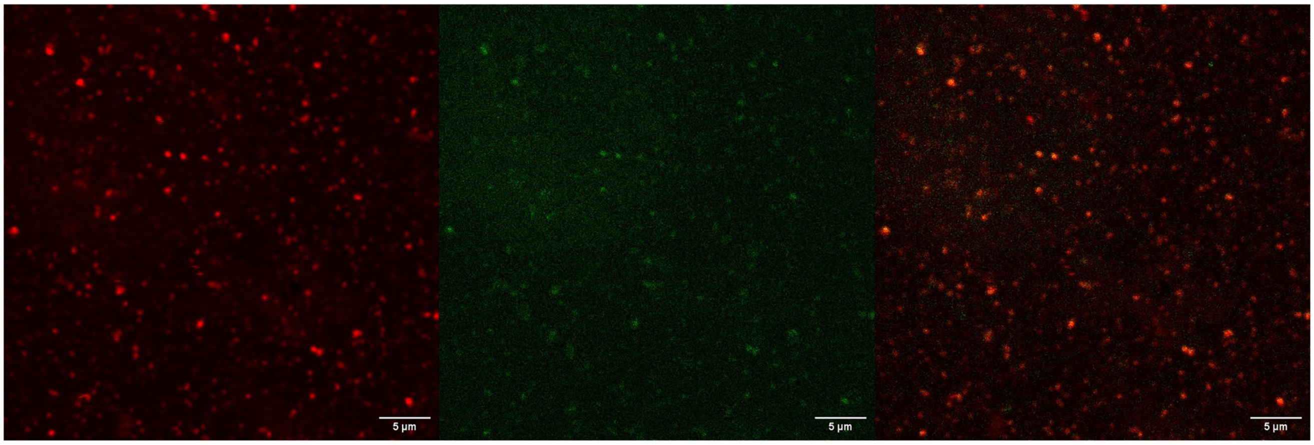

Figure 7. Representative LSCM images of purified CellMask-labelled CSM membranes from *E. coli*. (a) Fluorescence image showing the CSM membrane stained with a plasma membrane dye (CellMask Orange). (b) GFP fluorescence signal indicating the presence of encapsulated or surface-associated recombinant GFP. (c) Merged images. GFP fluorescence was recorded at λ_{ex} = 488 nm and λ_{em} = 495–550 nm. CellMask Orange was recorded at λ_{ex} = 546 nm and λ_{em} = 560–620 nm. Scale bar 5 µm.

EV contents can be modified *via* incubation, transfection, sonication, extrusion, freeze-thaw cycles, electroporation, or chemical treatments [33,48]. These approaches facilitate the loading of EVs with drugs, nucleic acids, and therapeutic molecules, highlighting their promise in targeted therapies [48].

While EVs hold significant biomedical potential, their extraction poses challenges due to the variability in quality and yield, complicating production and downstream processes [49]. Lipid vesicles help improve these parameters [50,51] but may trigger immune activation, aggregate easily, and require stabilizers [52]. Compared to natural vesicle isolation methods like differential centrifugation and density gradient ultracentrifugation, extrusion-based cell membrane-derived vesicles (CSMs) provide advantages by minimizing

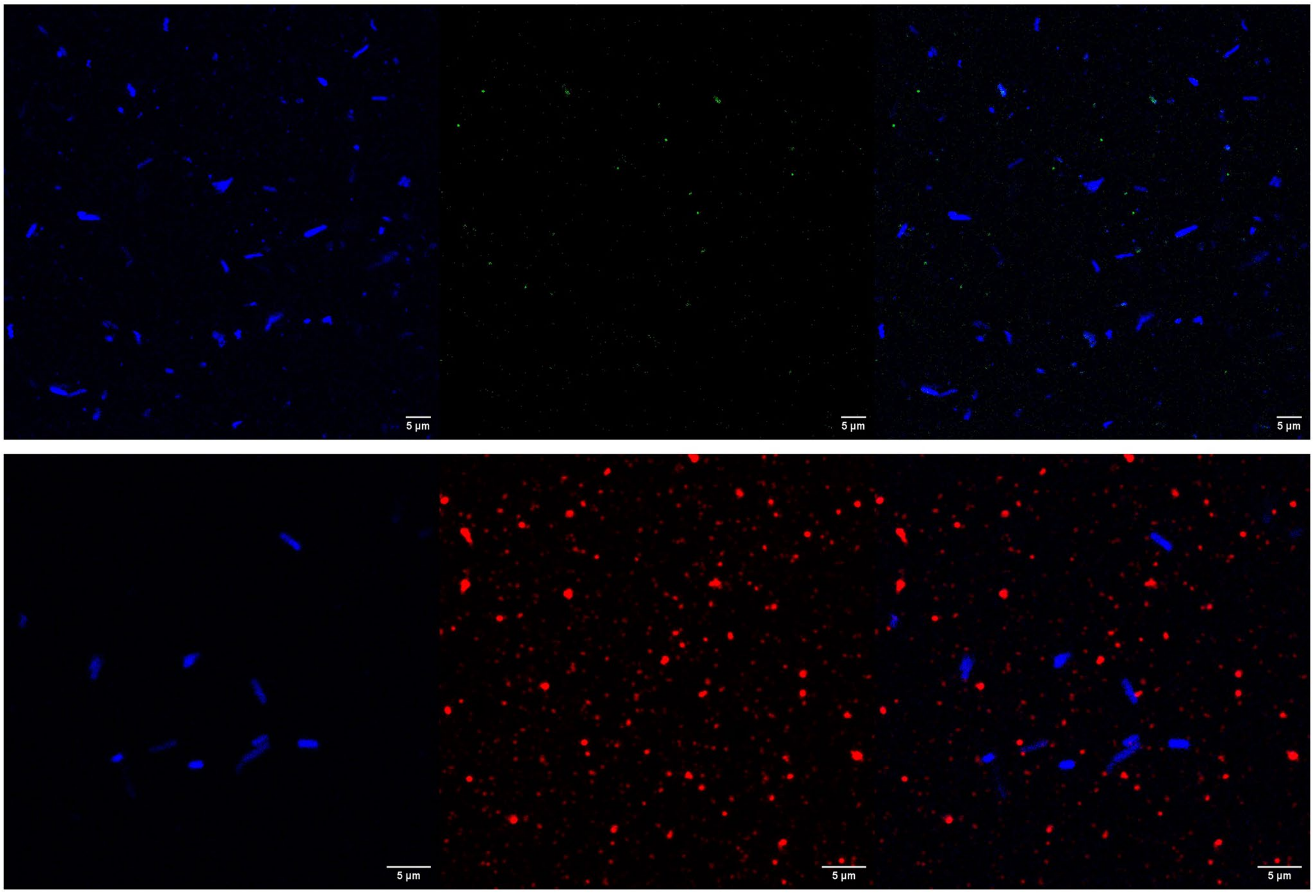

Figure 8. Visualization of GFP-labelled CSM interactions with *E. coli*. Upper row: *E. coli* + GFP-labelled CSMs (GFP, green; Hoechst, blue; Merge). Lower row: *E. coli* + CellMask-labelled CSMs (CellMask, red; Hoechst, blue; Merge). GFP fluorescence was recorded at λ_{ex} = 488 nm and λ_{em} = 495–550 nm. CellMask Orange was recorded at λ_{ex} = 546 nm and λ_{em} = 560–620 nm. Hoechst fluorescence was recorded at λ_{ex} = 405 nm and λ_{em} = 430–470 nm. Scale bar 5 µm.

heterogenicity observed in extracellular vesicles (EVs), such as exosomes, microvesicles, and apoptotic bodies. This heterogeneity complicates applications requiring precise control, such as drug delivery and diagnostics.

An alternative to natural vesicle isolation is using purified cell membranes subjected to extrusion processes, encapsulating proteins, nucleic acids, or drugs to form CSMs. Extrusion ensures a standardized, reproducible vesicle population in contrast to heterogeneous mixtures. Extrusion-based CDNVs [29] and nPMVs derived from chemically induced blebs have demonstrated standardized, high-yield production in mammalian systems [37]. Our workflow builds on these advances but differs in scope: (i) it applies a single parameterized sequence to both mammalian and bacterial membranes; (ii) it incorporates FACS-based subpopulation gating and IMAC cargo depletion directly into the workflow; and (iii) it reports harmonized DLS and thermal-stability readouts for cross-kingdom comparability. Recent organ-targeted implementations of mechanical extrusion are complementary to our approach [30].

Consistent with recent analyses of extrusion-prepared coreless CMVs, membrane orientation is expected to be mixed owing to stochastic wrapping; we therefore anticipate a distribution of right-side-out and inside-out vesicles in our preparations [53]. Although we did not profile specific HeLa markers here, engineered nanovesicles produced by extrusion are widely reported to inherit parental membrane proteins and preserve surface features relevant to uptake and homotypic interactions [25,26,29,54]. Membrane purification also reduces contaminants in EV preparations. Originally developed for synthetic liposome-based delivery, extrusion technology has been adapted for GMP-compliant active cell-derived vesicle production [31]. This study explores CSMs derived from eukaryotic and prokaryotic sources as biological delivery vehicles. Beyond engineered vesicles produced by extrusion, a large body of work has explored membrane-functionalized and hybrid nanocarriers that leverage cell-membrane biology for targeting, immune evasion, and uptake. Representative studies illustrate how membrane-informed designs and tumor-penetration strategies can enhance delivery performance, complementing our standardized, cross-kingdom CSM workflow [55,56]. Readers are referred to recent reviews on cell-membrane-coated nanoparticles for broader context on coating methods, interactions with biological membranes, and translational considerations [32,55,56].

In the protocol presented here, soluble his-tagged eGFP and eGFP/mRuby were mixed with the membrane pellet prior to extrusion, followed by post-extrusion cell sorting or IMAC depletion of free His-tagged protein. Given that eGFP/mRuby are soluble β-barrel fluorescent proteins with no transmembrane segments, spontaneous integration into the bilayer is unlikely without dedicated anchors or detergents; the most plausible outcomes are lumenal encapsulation and/or peripheral adsorption [57]. Consistent with analogous liposome systems that encapsulate GFP as an aqueous cargo, we avoid over-interpreting LSCM ring-like signals and treat them as qualitative. Future work will apply standard discriminators to characterize vesicle cargo, such as protease protection assays, sodium carbonate extraction to remove peripheral proteins. and limited trypsin accessibility to assess surface exposure.

The results of this study confirm that vesicles can be successfully formed by extruding membranes from both eukaryotic and prokaryotic cells. CSMs derived from HeLa and SH-SY5Y cells displayed uniform, GFP-labelled cup-shaped structures, as shown in LSCM images (Figure 1). However, cell sorting flow cytometry compromised the stability of SH-SY5Y-derived CSMs. Variations in membrane composition across cell lines likely account for variations in molecule diffusion, influencing sensitivity to purification. For instance, higher membrane fluidity in SH-SY5Y cells compared to HeLa cells may explain their reduced stability [58]. We speculate that the improved stability observed for HeLa–derived vesicles reflects differences in membrane lipid order/raft content rather than cargo composition per se. In SH-SY5Y cells, altering cholesterol/GM1 changes membrane physicochemical properties, consistent with raft-associated remodelling [59]. Membrane order is a measurable biophysical parameter in living cells by Laurdan/C-Laurdan imaging [60]. Furthermore, membrane order/fluidity can modulate vesicle-membrane interactions and uptake [61]. In this context, cholesterol enrichment is known to hinder the passive penetration of amphiphiles through fluid bilayers [62]. The size differences between vesicles further suggest that CSM physicochemical properties depend on membrane origin (Figures 1 and 3).

Discrepancies between Dynamic Light Scattering (DLS) and Transmission Electron Microscopy (TEM) methodologies are expected due to fundamental differences in measurement principles. DLS reports the intensity-weighted hydrodynamic diameter (R_h), encompassing the hydration shell or soft corona, and inherently exhibits a strong bias towards larger species because scattered light intensity is proportional to particle diameter raised approximately to the sixth power ($I \propto d$^6) [63,64]. In contrast, cryo-TEM measures the projected physical diameter of vitrified particles, a result sensitive to segmentation criteria and potential artefacts from sample preparation [65]. Consistent with current standards in the Extracellular Vesicle (EV) field [66], accurate particle sizing must be supported by multiple orthogonal methods such as single-particle techniques (Nanoparticle Tracking Analysis -NTA, Microfluidic Resistive Pulse Sensing (MRPS/TRPS)) alongside EM, rather than relying on any single technique [64,65]. Consequently, we avoid definitive claims of 'monodisperse' (a descriptor rarely met in biological systems, where Polydispersity Index (PDI) <0.05 is uncommon) [63], choosing instead to describe our preparations as 'narrowly distributed under our conditions', pending quantitative single-particle validation. Temperature stability tests revealed that CSMs remained structurally intact across 4-75 °C. Similar stability studies have shown that glycolipids can enhance liposomal thermal stability [67]. Although we did not perform a storage time-course, prior studies on engineered/extruded nanovesicles report that short-term storage at 4 °C preserves size and dispersion with limited drift, whereas long-term storage is improved by cryopreservation (e.g. addition of a cryoprotectant) and by minimizing freeze–thaw cycles. In our workflow, vesicles were used immediately after preparation or temporarily held at 4 °C in the dark, and repeated freeze–thawing was avoided [37,68]. Our focus is on establishing a standardized, cross-kingdom protocol, characterized by clearly defined parameters such as pore size tailored to each kingdom, multi-pass extrusion at 4 °C, and isotonic buffering, along with integrated purification steps. This approach is designed to ensure reproducibility of yields, particle sizes (measured *via* DLS), and morphology (assessed *via* cryo-TEM), without the need for specialized hardware. The efficiency of IMAC/FACS in removing non-encapsulated cargo was not quantified in the current study. Future work will incorporate SDS-PAGE and Western blot-based mass balance analyses, as well as protease protection assays, to enable a more accurate assessment of encapsulation efficiency.

Interaction assays with HeLa cells showed that CSMs rapidly bind and interact with cell membranes, showing cell-associated GFP signal compatible with internalization soon after incubation. Cellular mechanisms for nanoparticle internalization have been described to occur rapidly [69]. Time-lapse imaging was not conducted for Figure 5; uptake was depicted through endpoint images only. This efficient interaction is consistent with membrane fusion events observed in bacterial vesicle studies, such as Yaron et al. (2000), where *E. coli* O157 vesicles successfully transferred virulence factors to recipient cells. However, unlike natural bacterial vesicles, our CSMs did not enable plasmid DNA transformation of *E. coli,* suggesting that Gram-negative bacterial vesicles originating from the outer membrane may possess specific mechanisms for nucleic acid encapsulation and delivery, which are likely absent in extruded CSMs. Future work will implement extracellular quenching (trypan-blue/anti-GFP), acid/pronase washes and temperature/endocytosis controls, and protease-protection ± mild detergent to distinguish internal vs surface-bound cargo.

While eukaryotic CSMs appeared as monodisperse populations in DLS analysis (Figure 3a, c), bacterial CSMs showed greater dispersion under the same experimental conditions (Figure 3e). Cryo-TEM images confirmed monodisperse structures around 100 nm (Figure 4), but DLS indicated larger sizes (Figure 3e), likely due to vesicle clustering or aggregation in solution, a phenomenon that has been previously documented in studies on synthetic and natural vesicle systems [67]. The discrepancy stems from differences in technique: Cryo-TEM captures individual, unhydrated vesicles in frozen states, while DLS measures hydrodynamic diameter, which reflects hydration layers, deformation, and potential aggregation. Factors such as ionic strength and temperature during DLS may further promote apparent size increases, as seen in thermal stability tests (Figure 3). Optimizing buffer conditions and centrifugation protocols could minimize aggregation and better align DLS with Cryo-TEM data. Although negative-stain TEM can provide higher contrast, it may distort vesicle shape and apparent membrane thickness; for this workflow we prioritized cryo-TEM to preserve native features.

Moreover, the lower concentration of bacterial CSM in the cryo-TEM due to additional Ni^{2+} affinity purification (see section Cellsomes visualization in Cryo-TEM) may also explain size differences. Furthermore, vesicle-vesicle interactions might hinder cell transformation, further suggesting that current methods for generating bacterial CSMs by extrusion need significant refinement. Using *E. coli* strains with altered peptidoglycan, such as ΔnlpI mutants or cultures supplemented with 1% glycine, can enhance vesicle production and plasmid loading [70]. Selecting small, high-copy plasmids further increases incorporation [71]. Post-formation approaches, including electroporation or cell-penetrating peptides, markedly improve nucleic acid encapsulation [72]. Finally, optimizing extrusion with suitable buffers, alongside stabilizers like trehalose, helps maintain vesicle integrity and functionality [73].

Natural OMVs can package plasmid/genomic DNA and mediate horizontal gene transfer (HGT) between bacteria under defined conditions. Reports include several Gram-negative species where OMVs carry plasmids and transfer them to cell recipients [74–78]. Mechanistically, OMV biogenesis and composition (LPS architecture, outer-membrane proteins, periplasmic content) are thought to support docking, fusion, or uptake pathways [70,79]. In contrast, extruded CSMs, assembled from disrupted membranes with mixed orientation, may lack the curated outer-membrane landscape and biogenesis-linked factors that favour DNA delivery, which could explain the absence of transformants observed here (Figure 8). We also note that our plasmids are relatively large and highly supercoiled polyanions; without cation bridging (e.g. Ca^{2+}/Mg^{2+}) or fusogenic cues, successful release across the Gram-negative envelope is unlikely. Future directions may involve outer membrane characterization by optimizing sample preparation to enrich outer membrane fractions and lipopolysaccharides (LPS), including the use of specific outer membrane protein markers [79]. Incubation protocols could be refined by incorporating Ca^{2+} and Mg^{2+} ions to reduce electrostatic repulsion [80]. Additionally, insights from hypervesiculating mutants such as ΔnlpI and ΔtolA may inform vesicle composition strategies [70]. Finally, DNase protection assays, with and without detergent treatment, could be employed to confirm the presence of intravesicular DNA [79]. Together, these considerations suggest that OMV-like delivery is not recapitulated by simple extrusion and that CSM-mediated bacterial transformation will require further engineering. Challenges in producing transformation-competent bacterial CSMs *via* extrusion may also stem from contamination with cellular components like peptidoglycans or inner membrane remnants. Enhancing the production process by incorporating or mimicking key features of natural vesicles could improve fusion and delivery efficiency.

Our findings introduce an alternative strategy for generating cell membrane–derived vesicles as a substitute for naturally secreted extracellular vesicles. This approach addresses some of the inherent variability and limited scalability associated with native vesicle production, offering a more controllable platform for biomimetic delivery. By leveraging extrusion-based methods, we preserve key membrane components that may contribute to biological compatibility, while enabling customization of cargo loading. These features position extruded vesicles within the broader landscape of synthetic and semi-synthetic delivery systems, where the balance between structural fidelity and functional tuneability remains a central challenge. Future work should explore how this strategy compares to other biomimetic carriers in terms of stability, targeting, and immunogenicity, thereby clarifying its potential role in therapeutic and diagnostic applications.

In conclusion, while extruded CSMs show strong potential for biomedical uses, including drug delivery protein transport, and imaging agents, their effectiveness in genetic material transfer remains limited. Comparing these results with previous studies on natural bacterial vesicles emphasizes the unique attributes that natural vesicles possess in gene transfer, attributes that CSMs could potentially be engineered to replicate. Future research should focus on refining CSM composition and encapsulation methods to fully exploit their therapeutic potential.

Acknowledgements

We also thank the ICTS 'NANBIOSIS', specifically the Protein Production Platform of CIBER-BBN/IBB at the UAB technical service (http://www.nanbiosis.es/unit/u1-protein-production-platform-ppp/), and the SMiDRX microscopy and SCAC cytometry services at the Universitat Autònoma de Barcelona (https://www.uab.cat/web/research/scientific-technical-services/scientific-and-technical-services–1345667278676.html). Additionally, we acknowledge the support of the Confocal Microscopy Facility at the Centre for Research in Agricultural Genomics (CRAG) (https://www.cragenomica.es/facilities/microscopy-and-imaging) and the Centre for Microscopy Characterisation and Analysis at the University of Western Australia, a Microscopy Australia (ROR: 042mm0k03) facility enabled by NCRIS. Furthermore, the authors appreciate the support from the Ministerio de Universidades, Spain, through the FPU fellowship (FPU20/02260) and the Short Stays and Temporary Transfers program for FPU beneficiaries 2023 (EST23/00100), both awarded to JAG., which have been instrumental in carrying out this research. The content of this manuscript has previously appeared in the doctoral thesis of JAG., titled 'Advancing Antimicrobial and Vaccine Delivery Systems: Innovations in Protein Nanoparticles, Encapsulation Techniques, and Targeted Therapeutic Approaches'. This thesis is not currently available online but contains foundational research contributing to the development of this article.

Author contributions

JAG, LS, and CC performed the experimental work. JAG, AV, and NFM contributed to the design and supervision of the study. JAG and LS developed the overall study concept. JAG and NFM prepared the initial draft of the manuscript, which was subsequently reviewed and edited by all authors. All authors read and approved the final manuscript.

Disclosure statement

No potential conflict of interest was reported by the author(s).

Funding

This work was supported by the Spanish Ministry of Science, Innovation, and Universities (MICIU) and the State Research Agency (AEI) under grant number PID2019-107298RB-C22, co-funded by the European Union 'NextGenerationEU'/PRTR. We also appreciate the funding received from the Instituto de Salud Carlos III through the 'Acciones CIBER' initiative. The authors extend their gratitude to the Networking Research Center on Bioengineering, Biomaterials, and Nanomedicine (CIBER-BBN), funded by the VI National R&D&I Plan 2008–2011, Iniciativa Ingenio 2010, and the Consolider Program, with support from the European Regional Development Fund. Authors also thank Catalan AGAUR (2021 SGR00092).

ORCID

Jan Atienza-Garriga http://orcid.org/0000-0001-5537-3566
Luke Smithers http://orcid.org/0000-0002-4512-9401
Crystal Cooper http://orcid.org/0000-0002-5247-1168
Alice Vrielink http://orcid.org/0000-0001-8197-3725
Neus Ferrer-Miralles http://orcid.org/0000-0003-2981-3913

Data availability statement

All raw datasets underlying the figures presented in this study are available at the CORA Repositori de Dades de Recerca https://doi.org/10.34810/data1795.

References

[1] Tkach M, Théry C. Communication by extracellular vesicles: where we are and where we need to go. Cell. 2016;164(6):1226–1232. doi: 10.1016/j.cell.2016.01.043.

[2] Fang RH, Gao W, Zhang L. Targeting drugs to tumours using cell membrane-coated nanoparticles. Nat Rev Clin Oncol. 2023;20(1):33–48. doi: 10.1038/s41571-022-00699-x.

[3] Doyle LM, Wang MZ. Overview of extracellular vesicles, their origin, composition, purpose, and methods for exosome isolation and analysis. Cells. 2019;8(7):727. doi: 10.3390/cells8070727.

[4] Kakarla R, Hur J, Kim YJ, et al. Apoptotic cell-derived exosomes: messages from dying cells. Exp Mol Med. 2020;52(1):1–6. doi: 10.1038/s12276-019-0362-8.

[5] Robbins PD, Morelli AE. Regulation of immune responses by extracellular vesicles. Nat Rev Immunol. 2014;14(3):195–208. doi: 10.1038/nri3622.

[6] Chang WH, Cerione RA, Antonyak MA. Extracellular vesicles and their roles in cancer progression. Methods Mol Biol. 2021;2174:143-170. doi: 10.1007/978-1-0716-0759-6_10.

[7] Roefs MT, Sluijter JPG, Vader P. Extracellular vesicle-associated proteins in tissue repair. Trends Cell Biol. 2020;30(12):990–1013. doi: 10.1016/j.tcb.2020.09.009.

[8] Beveridge TJ. Structures of gram-negative cell walls and their derived membrane vesicles. J Bacteriol. 1999;181(16):4725–4733. doi: 10.1128/JB.181.16.4725-4733.1999.

[9] Lee E-Y, Choi D-Y, Kim D-K, et al. Gram-positive bacteria produce membrane vesicles: proteomics-based characterization of *Staphylococcus aureus*-derived membrane vesicles. Proteomics. 2009;9(24):5425–5436. doi: 10.1002/pmic.200900338.

[10] Xiu L, Wu Y, Lin G, et al. Bacterial membrane vesicles: orchestrators of interkingdom interactions in microbial communities for environmental adaptation and pathogenic dynamics. Front Immunol. 2024;15:1371317. doi: 10.3389/fimmu.2024.1371317.

[11] Gan Y, Zhao G, Wang Z, et al. Bacterial membrane vesicles: physiological roles, infection immunology, and applications. Adv Sci. 2023;10(25):2301357–2301357. doi: 10.1002/advs.202301357.

[12] Guo Y, Zhang Y, Li JL, et al. Diffusible signal factor-mediated quorum sensing plays a central role in coordinating gene expression of *Xanthomonas citri* subsp. citri. Mol Plant Microbe Interact. 2012;25(2):165–179. doi: 10.1094/MPMI-07-11-0184.

[13] Xu P, He J, Xu T, et al. Synergistic integration of extracellular vesicles and metal-organic frameworks: unlocking new opportunities in disease diagnosis and therapy. Theranostics. 2025;15(16):8609–8638. doi: 10.7150/thno.113474.

[14] Guo C, Lin L, Wang Y, et al. Nano drug delivery systems for advanced immune checkpoint blockade therapy. Theranostics. 2025;15(11):5440–5480. doi: 10.7150/thno.112475.

[15] Rakshit T, Pal S. Extracellular vesicles for drug delivery and theranostics in vivo. JACS Au. 2024;4(2):318–327. doi: 10.1021/jacsau.3c00611.

[16] Meng W, He C, Hao Y, et al. Prospects and challenges of extracellular vesicle-based drug delivery system: considering cell source. Drug Deliv. 2020;27(1):585–598. doi: 10.1080/10717544.2020.1748758.

[17] Feng X, Shen A, Zhang W, et al. High-throughput capture and in situ protein analysis of extracellular vesicles by chemical probe-based array. Nat Protoc. 2025;20(4):1057–1081. doi: 10.1038/s41596-024-01082-z.

[18] Wang M, Liu X, Song J, et al. Extracellular vesicle encapsulated mesoporous molecularly imprinted silica for peptide drug delivery. Colloids Surf B Biointerfaces. 2025;255:114971. doi: 10.1016/j.colsurfb.2025.114971.

[19] Zhou J, et al. Epitope imprinting of phospholipids by oriented assembly at the oil/water interface for the selective recognition of plasma membranes. Ang Chem – Int Ed. 2023;62.

[20] Cheng X, Miao Y, Zhou J, et al. Cell-penetrating drug carrier by molecular recognition of sphingomyelin on plasma membranes. Langmuir. 2024;40(19):9975–9984. doi: 10.1021/acs.langmuir.4c00101.

[21] Chen L, Yu W, Zhao J, et al. Molecular imprinting of phospholipids for targeted cell and exosome recognition. Anal Chem. 2025;97(18):9953–9960. doi: 10.1021/acs.analchem.5c00686.

[22] Feng X, Iliuk A, Zhang X, et al. Supramolecular exosome array for efficient capture and in situ detection of protein biomarkers. Anal Chem. 2023;95(5):2812–2821. doi: 10.1021/acs.analchem.2c04190.

[23] Feng X, Jia S, Ali MM, et al. Proteomic discovery and array-based validation of biomarkers from urinary exosome by supramolecular probe. J Proteome Res. 2023;22(7):2516–2524. doi: 10.1021/acs.jproteome.3c00063.

[24] Soprano E, Alvarez A, Pelaz B, et al. Plasmonic cell-derived nanocomposites for light-controlled cargo release inside living cells. Adv Biosyst. 2020;4(3): e1900260. doi: 10.1002/adbi.201900260.

[25] Wang X, Hu S, Zhu D, et al. Comparison of extruded cell nanovesicles and exosomes in their molecular cargos and regenerative potentials. Nano Res. 2023;16(5): 7248–7259. doi: 10.1007/s12274-023-5374-3.

[26] Wang X, Hu S, Li J, et al. Extruded mesenchymal stem cell nanovesicles are equally potent to natural extracellular vesicles in cardiac repair. ACS Appl Mater Interfaces. 2021;13(47):55767–55779. doi: 10.1021/acsami.1c08044.

[27] Kim S, Lee J, Park J. Cellular membrane-derived nanovesicles expressing hCD64 for targeting prostate cancer. ACS Appl Bio Mater. 2024;7(10):6941–6949. doi: 10.1021/acsabm.4c01045.

[28] Li W, Zhang H, Chen L, et al. Cell membrane-derived nanovesicles as extracellular vesicle-mimetics in wound healing. Mater Today Bio. 2025;31:101595. doi: 10.1016/j.mtbio.2025.101595.

[29] Wen Y, Fu Q, Soliwoda A, et al. Cell-derived nanovesicles prepared by membrane extrusion are good substitutes for natural extracellular vesicles. Extracell Vesicle. 2022;1:100004. doi: 10.1016/j.vesic.2022.100004.

[30] Liu Y, Ling Y, Tai W. Mechanical extrusion of the plasma membrane to generate ectosome-mimetic nanovesicles for lung targeting. Mol Pharm. 2025;22(1):304–315. doi: 10.1021/acs.molpharmaceut.4c00927.

[31] Lau H-C, Han DW, Park J, et al. GMP-compliant manufacturing of biologically active cell-derived vesicles produced by extrusion technology. J Extracell Biol. 2022;1(12):e70. doi: 10.1002/jex2.70.

[32] Liu H, Su YY, Jiang XC, et al. Cell membrane-coated nanoparticles: a novel multifunctional biomimetic drug delivery system. Drug Deliv Transl Res. 2023;13(3):716–737. doi: 10.1007/s13346-022-01252-0.

[33] Zhang W, Wang J, Ngo L, et al. Recent advances in cancer cell membrane-based nanoparticles and cancer cell-derived small extracellular vesicles as drug delivery platforms. Adv Nanobiomed Res. 2025;5(6):2500008. doi: 10.1002/anbr.202500008.

[34] Goh WJ, Zou S, Ong WY, et al. Bioinspired cell-derived nanovesicles versus exosomes as drug delivery systems: a cost-effective alternative. Sci Rep. 2017;7(1):14322. doi: 10.1038/s41598-017-14725-x.

[35] Prasad R, Mendes BB, Gorain M, et al. Bioinspired and biomimetic cancer-cell-derived membrane nanovesicles for preclinical tumor-targeted nanotheranostics. Cell Rep Phys Sci. 2023;4(11):101648. doi: 10.1016/j.xcrp.2023.101648.

[36] Liu X, Xiao C, Xiao K. Engineered extracellular vesicles-like biomimetic nanoparticles as an emerging platform for targeted cancer therapy. J Nanobiotechnol. 2023;21(1). doi: 10.1186/s12951-023-02064-1.

[37] Alter CL, Detampel P, Schefer RB, et al. High efficiency preparation of monodisperse plasma membrane derived extracellular vesicles for therapeutic applications. Commun Biol. 2023;6(1):478. doi: 10.1038/s42003-023-04859-2.

[38] Le QV, Lee J, Lee H, et al. Cell membrane-derived vesicles for delivery of therapeutic agents. Acta Pharm Sin B. 2021;11(8):2096–2113. doi: 10.1016/j.apsb.2021.01.020.

[39] Wagner S, Klepsch MM, Schlegel S, et al. Tuning Escherichia coli for membrane protein overexpression.

Proc Natl Acad Sci U S A. 2008;105(38):14371–14376. doi: 10.1073/pnas.0804090105.

[40] Gao J, Qian H, Guo X, et al. The signal peptide of Cry1Ia can improve the expression of eGFP or mCherry in *Escherichia coli* and *Bacillus thuringiensis* and enhance the host's fluorescent intensity. Microb Cell Fact. 2020;19(1):112. doi: 10.1186/s12934-020-01371-8.

[41] Carratalá JV, Atienza-Garriga J, López-Laguna H, et al. Enhanced recombinant protein capture, purity and yield from crude bacterial cell extracts by N-Lauroylsarcosine-assisted affinity chromatography. Microb Cell Fact. 2023;22(1):81. doi: 10.1186/s12934-023-02081-7.

[42] Harvey BT, Fu X, Li L, et al. Dendritic cell membrane-derived nanovesicles for targeted T cell activation. ACS Omega. 2022;7(50):46222–46233. doi: 10.1021/acsomega.2c04420.

[43] Wu JY, Li YJ, Hu XB, et al. Preservation of small extracellular vesicles for functional analysis and therapeutic applications: a comparative evaluation of storage conditions. Drug Deliv. 2021;28(1):162–170. doi: 10.1080/10717544.2020.1869866.

[44] Yang Y, Liu M, Wang T, et al. An optimized transformation protocol for *Escherichia coli* BW3KD with supreme DNA assembly efficiency. Microbiol Spectr. 2022;10(6): e0249722. doi: 10.1128/spectrum.02497-22.

[45] Toyofuku M, Schild S, Kaparakis-Liaskos M, et al. Composition and functions of bacterial membrane vesicles. Nat Rev Microbiol. 2023;217):415–430. doi: 10.1038/s41579-023-00875-5.

[46] Xu Y, Xie C, Liu Y, et al. An update on our understanding of Gram-positive bacterial membrane vesicles: discovery, functions, and applications. Front Cell Infect Microbiol. 2023;131273813. doi: 10.3389/fcimb.2023.1273813.

[47] Schwechheimer C, Kuehn MJ. Outer-membrane vesicles from Gram-negative bacteria: biogenesis and functions. Nat Rev Microbiol. 2015;13(10):605–619. doi: 10.1038/nrmicro3525.

[48] Fu S, Wang Y, Xia X, et al. Exosome engineering: current progress in cargo loading and targeted delivery. NanoImpact. 2020;20:100261. doi: 10.1016/j.impact.2020.100261.

[49] Jia Y, Yu L, Ma T, et al. Small extracellular vesicles isolation and separation: current techniques, pending questions and clinical applications. Theranostics. 2022;12(15): 6548–6575. doi: 10.7150/thno.74305.

[50] Allen TM, Cullis PR. Liposomal drug delivery systems: from concept to clinical applications. Adv Drug Deliv Rev. 2013;65(1):36–48. doi: 10.1016/j.addr.2012.09.037.

[51] Sercombe L, Veerati T, Moheimani F, et al. Advances and challenges of liposome assisted drug delivery. Front Pharmacol. 2015;6:286. doi: 10.3389/fphar.2015.00286.

[52] Zahednezhad F, Saadat M, Valizadeh H, et al. Liposome and immune system interplay: challenges and potentials. J Control Release. 2019;305:194–209. doi: 10.1016/j.jconrel.2019.05.030.

[53] Ye J, Xu F, Xu Z, et al. Sorting extrusion-prepared coreless cell membrane vesicles of mixed orientations by functional DNA Probes. JACS Au. 2025;5(4):1728–1737. doi: 10.1021/jacsau.4c01251.

[54] Liew WJM, Alkaff SA, Leong SY, et al. Cell membrane- and extracellular vesicle-coated chitosan methacrylate-tripolyphosphate nanoparticles for RNA delivery. Int J Mol Sci. 2024;25(24):13724. doi: 10.3390/ijms252413724.

[55] Duan Z, Luo Q, Dai X, et al. Synergistic therapy of a naturally inspired glycopolymer-based biomimetic nanomedicine harnessing tumor genomic instability. Adv Mater. 2021;33(45):2104594. doi: 10.1002/adma.202104594.

[56] Gu L, Duan Z, Li X, et al. Enzyme-triggered deep tumor penetration of a dual-drug nanomedicine enables an enhanced cancer combination therapy. Bioact Mater. 2023;26:102–115. doi: 10.1016/j.bioactmat.2023.02.015.

[57] Yang K, Tang M, Chang H-H, et al. Mannosylation of pH-sensitive liposomes promoted cytoplasmic delivery of protein to macrophages: green fluorescent protein (GFP) performed as an endosomal escape tracer. Pharm Dev Technol. 2021;26(9):1000–1009. doi: 10.1080/10837450.2021.1969406.

[58] Huang S, Lim SY, Gupta A, et al. Plasma membrane organization and dynamics is probe and cell line dependent. Biochim Biophys Acta Biomembr. 2017;1859(9 Pt A):1483–1492. doi: 10.1016/j.bbamem.2016.12.009.

[59] Evangelisti E, Cecchi C, Cascella R, et al. Membrane lipid composition and its physicochemical properties define cell vulnerability to aberrant protein oligomers. J Cell Sci. 2012;125(Pt 10):2416–2427. doi: 10.1242/jcs.098434.

[60] Levitan I. Evaluating membrane structure by Laurdan imaging: disruption of lipid packing by oxidized lipids. in. Curr Top Membr. 2021;88:235–256. doi: 10.1016/bs.ctm.2021.10.003.

[61] Liu W, Gao T, Li N, et al. Vesicle fusion and release in neurons under dynamic mechanical equilibrium. iScience. 2024;27(5):109793. doi: 10.1016/j.isci.2024.109793.

[62] Canepa E, et al. Cholesterol Hinders the Passive Uptake of Amphiphilic Nanoparticles into Fluid Lipid Membranes. J Phys Chem Lett. 2021;12: 8583–8590. doi: 10.1021/acs.jpclett.1c02077.

[63] Stetefeld J, McKenna SA, Patel TR. Dynamic light scattering: a practical guide and applications in biomedical sciences. Biophys Rev. 2016;8(4):409–427. doi: 10.1007/s12551-016-0218-6.

[64] Filipe V, Hawe A, Jiskoot W. Critical evaluation of nanoparticle tracking analysis (NTA) by NanoSight for the measurement of nanoparticles and protein aggregates. Pharm Res. 2010;27(5):796–810. doi: 10.1007/s11095-010-0073-2.

[65] van der Pol E, Coumans FAW, Grootemaat AE, et al. Particle size distribution of exosomes and microvesicles determined by transmission electron microscopy, flow cytometry, nanoparticle tracking analysis, and resistive pulse sensing. Journal of Thrombosis and Haemostasis. 2014;12(7):1182–1192. doi: 10.1111/jth.12602.

[66] Welsh JA, Goberdhan DC, O'Driscoll L, et al. MISEV2023: an updated guide to EV research and applications. J Extracell Vesicles. 2024;13(2):e12416. doi: 10.1002/jev2.12416.

[67] Yi X, Gao S, Gao X, et al. Glycolipids improve the stability of liposomes: the perspective of bilayer membrane structure. Food Chem. 2023;412:135517. doi: 10.1016/j.foodchem.2023.135517.

[68] Božič D, Hočevar M, Kisovec M, et al. Stability of erythrocyte-derived nanovesicles assessed by light scattering and electron microscopy. Int J Mol Sci. 2021;22(23):12772. doi: 10.3390/ijms222312772.

[69] Richards CJ, Burgers TCQ, Vlijm R, et al. Rapid internalization of nanoparticles by human cells at the single particle level. ACS Nano. 2023;17(17):16517–16529. doi: 10.1021/acsnano.3c01124.

[70] Aktar S, Okamoto Y, Ueno S, et al. Incorporation of plasmid DNA into bacterial membrane vesicles by peptidoglycan defects in *Escherichia coli*. Front Microbiol. 2021;12:747606. doi: 10.3389/fmicb.2021.747606.

[71] Tran F, Boedicker JQ. Plasmid characteristics modulate the propensity of gene exchange in bacterial vesicles. J Bacteriol. 2019;201(7):e00430. doi: 10.1128/JB.00430-18.

[72] Nebogatova J, Härk HH, Puskar A, et al. A method for using cell-penetrating peptides for loading plasmid DNA into secreted extracellular vesicles. Biomolecules. 2023;13(12):1751. doi: 10.3390/biom13121751.

[73] Ilahibaks NF, Ardisasmita AI, Xie S, et al. TOP-EVs: technology of protein delivery through extracellular vesicles is a versatile platform for intracellular protein delivery. J Controlled Release. 2023;355:579–592. doi: 10.1016/j.jconrel.2023.02.003.

[74] Renelli M, Matias V, Lo RY, et al. DNA-containing membrane vesicles of *Pseudomonas aeruginosa* PAO1 and their genetic transformation potential. Microbiology (N Y). 2004;150(7):2161–2169. doi: 10.1099/mic.0.26841-0.

[75] Li P, Luo W, Xiang T-X, et al. Horizontal gene transfer via OMVs co-carrying virulence and antimicrobial-resistant genes is a novel way for the dissemination of carbapenem-resistant hypervirulent *Klebsiella pneumoniae*. Front Microbiol. 2022;13:945972. doi: 10.3389/fmicb.2022.945972.

[76] Fulsundar S, Harms K, Flaten GE, et al. Gene transfer potential of outer membrane vesicles of *Acinetobacter baylyi* and effects of stress on vesiculation. Appl Environ Microbiol. 2014;80(11):3469–3483. doi: 10.1128/AEM.04248-13.

[77] Shen Z, Qin J, Xiang G, et al. Outer membrane vesicles mediating horizontal transfer of the epidemic blaOXA-232 carbapenemase gene among Enterobacterales. Emerg Microbes Infect. 2024;13(1):2290840. doi: 10.1080/22221751.2023.2290840.

[78] Johnston EL, Zavan L, Bitto NJ, et al. Planktonic and biofilm-derived *Pseudomonas aeruginosa* outer membrane vesicles facilitate horizontal gene transfer of plasmid DNA. Microbiol Spectr. 2023;11(2):e0517922. doi: 10.1128/spectrum.05179-22.

[79] Dell'Annunziata F, Folliero V, Giugliano R, et al. Gene transfer potential of outer membrane vesicles of gram-negative bacteria. IJMS. 2021;22(11):5985. doi: 10.3390/ijms22115985.

[80] Asif A, Mohsin H, Tanvir R, et al. Revisiting the mechanisms involved in calcium chloride induced bacterial transformation. Front Microbiol. 2017;8:2169. doi: 10.3389/fmicb.2017.02169.